

Bistable action with hybrid plasmonic Bragg-grating resonators

Thomas Christopoulos · Georgios Sinatkas ·
Odysseas Tsilipakos · Emmanouil E. Kriezis

Received: date / Accepted: date

Abstract Optical bistability with a hybrid silicon-plasmonic configuration consisting of a nonlinear Bragg-grating resonator side-coupled with a bus waveguide is theoretically investigated. The nonlinear response is studied with a modeling framework combining perturbation theory and temporal coupled-mode theory, fed with three-dimensional finite element method simulations. For the CW case, a general closed-form expression describing the nonlinear response is derived, valid for finite intrinsic quality factors and arbitrary coupling conditions. This generalization is necessary for studying plasmonic resonators which are inherently lossy. The effect of the parameters entering in the expression on the bistability curve is thoroughly investigated and the physical system is accordingly designed so as to exhibit minimum power threshold and an extinction ratio between bistable states exceeding 10 dB. Finally, the temporal dynamics are assessed. The system can toggle between bistable states in approximately 2 ps and is thus suitable for ultrafast memory/switching applications.

Keywords Nonlinear optics · Optical bistability · Plasmonics · Hybrid plasmonic waveguides · Bragg-grating resonators

PACS 42.65.Pc · 42.82.-m

1 Introduction

Nonlinear phenomena in guided-wave plasmonics are being intensively investigated, due to their potential for implementing tunable/dynamic integrated components (Kauranen and Zayats 2012). In particular, phenomena based on the third order susceptibility, $\chi^{(3)}$, can be a favorable approach, since they feature ultrafast response and allow for all-optical operation. Interestingly, the combination of nonlinearity and optical feedback in resonant nonlinear structures can lead to bistable behavior. In turn, this offers a route towards implementing memory, switching or logic-gate functions (Tanabe et al 2005; Almeida and Lipson 2004; Xu and Lipson 2007). What is more, the power requirements compared to nonresonant,

T. Christopoulos · G. Sinatkas · O. Tsilipakos · E. E. Kriezis
Department of Electrical and Computer Engineering, Aristotle University of Thessaloniki, GR-54125, Greece
Tel.: +30-2310-996362, Fax: +30-2310-996312
E-mail: otsilipa@auth.gr

directional coupler approaches (Milián and Skryabin 2011; Kriesch et al 2012; Ptilakis and Kriezis 2013) can be greatly reduced, since the intensity build-up in the resonator translates to high power densities enhancing nonlinear effects.

To date, bistability studies in plasmonics have mainly revolved around two-dimensional geometries with the metal-insulator-metal (MIM) waveguide (Pannipitiya et al 2011; Wang et al 2011; Xiang et al 2014; Shiu et al 2014). Addressing the need for practical, three-dimensional bistable components, we have recently examined the manifestation of optical bistability with nonlinear traveling-wave (disk) resonators made of hybrid plasmonic waveguides (Tsilipakos and Kriezis 2014). The presence of the resonator has led to reduced input power requirements, indicating the potential of bistable structures for practical applications. Standing-wave resonators can be also utilized for the task. In fact, such resonators can confine the optical mode in smaller volumes (since they do not rely on waveguide bending), therefore promising to further reduce the power threshold. For example, in the context of hybrid plasmonic waveguides, tight mode confinement has been demonstrated with 1D photonic crystal (nanobeam) resonators, investigated for lasing applications (Xu and Shi 2013). It is, thus, useful to investigate the prospect of standing-wave resonators for optical bistability and compare their performance with traveling-wave structures.

In this work, we focus on a nonlinear standing-wave resonator formed with Bragg reflectors. As in (Tsilipakos and Kriezis 2014), we base the physical implementation on a nonlinear hybrid plasmonic waveguide, which favors the manifestation of nonlinear effects through an advantageous combination of nanoscale confinement and relatively low loss. The resonator is side-coupled to the waveguide, since this coupling scheme is known to result in higher extinction ratios (ERs) between bistable states compared to direct coupling (Yanik et al 2003). The nonlinear response of the resonator-waveguide system is studied by means of a theoretical framework combining perturbation theory and temporal coupled-mode theory (CMT), fed with rigorous, full-wave simulations of the linear system conducted with the three-dimensional vectorial finite element method (3D-VFEM). Based on the simulation results, we identify the geometrical parameters leading to optimum performance and design the physical system accordingly. Subsequently, the performance is assessed in both CW and pulsed conditions.

The paper is organized as follows: The system under study is presented in Section 2. In Section 3 the theoretical framework is introduced and general *closed-form* equations describing the CW nonlinear response are derived, valid for finite intrinsic quality factors and arbitrary coupling conditions. The effect of the parameters entering in the theoretical model, namely, the detuning δ and intrinsic loss factor r_Q , on the bistability curve are investigated in Section 4. Based on the findings of this Section, we design the physical system in Section 5. Its performance in terms of required input power, extinction ratio between bistable states, and response time is assessed in Section 6. Finally, a conclusion and outlook is given in Section 7.

2 Nonlinear Bragg-grating resonator

The system considered is based on the nonlinear conductor-gap-silicon (NLCGS) waveguide introduced in (Ptilakis et al 2012). The waveguide cross-section is depicted in Fig. 1(a). It is similar to a standard CGS waveguide (Wu et al 2010), with the exception that a nonlinear polymer is occupying the low-index “gap” between high-index semiconductor and metal regions, instead of silica. More specifically, the polymer of choice is DDMEBT (Esembeon et al 2008), which apart from being highly nonlinear ($n_2 = 1.7 \times 10^{-17} \text{ m}^2/\text{W}$) has moreover

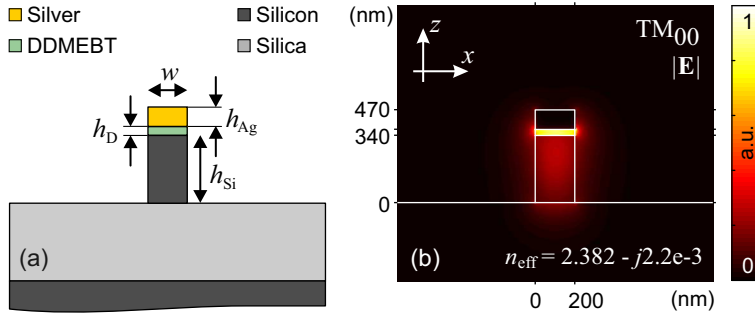


Fig. 1 (a) Cross-section of nonlinear CGS waveguide. The gap between silver and silicon layers is occupied by the nonlinear polymer DDMEBT. The heights of the three layers comprising the guiding ridge are $h_{Ag} = 100$ nm, $h_D = 30$ nm, and $h_{Si} = 340$ nm, respectively. The waveguide width w is 200 nm. (b) Distribution of electric field norm ($|\mathbf{E}|$) for the fundamental mode (TM_{00}) at $1.55 \mu\text{m}$.

proven compatible with nanophotonic integration (Koos et al 2009). The metal is silver, since it features lower resistive losses compared to gold, which is of paramount importance in nonlinear applications. The linear refractive indices for the considered materials at the telecom wavelength of $1.55 \mu\text{m}$ are $n_{\text{SiO}_2} = 1.45$, $n_{\text{Si}} = 3.48$, $n_D = 1.8$, and $n_{Ag} = 0.145 - j11.4$ (Johnson and Christy 1972).

Regarding geometrical parameters, the dimensions of the silicon core are $w \times h_{Si} = 200 \text{ nm} \times 340 \text{ nm}$, typical for CGS waveguides (Wu et al 2010). Importantly, the 340-nm height is customary for silicon photonic waveguides operating on the TM mode, thus facilitating the interfacing of the CGS waveguide with standard silicon photonic circuitry. The polymer layer is 30-nm high, in order to ensure tight mode confinement, while for the silver layer $h_{Ag} = 100$ nm.

The fundamental TM mode supported by the NLCGS waveguide is depicted in Fig. 1(b). More specifically, we plot the electric field norm, as obtained with a FEM eigenmode solver. The mode is almost entirely located inside the nanosized polymer layer. The effective mode area, calculated through $A_{\text{eff}} \triangleq (\iint |\mathbf{E}|^2 dx dy)^2 / \iint |\mathbf{E}|^4 dx dy$, is only $0.03 \mu\text{m}^2$. The effective index at $1.55 \mu\text{m}$ is $n_{\text{eff}} = 2.382 - j0.0022$, with the imaginary part corresponding to a propagation length (the e -folding distance of optical intensity) of $L_{\text{prop}} = 56 \mu\text{m}$. On the whole, the considered waveguide can provide subwavelength confinement while maintaining propagation loss at a relatively low level. Both of these traits are essential for the manifestation of nonlinear effects meaning that the NLCGS waveguide is well suited to our application.

The NLCGS-based standing-wave resonator structure examined is depicted in Fig. 2. A cavity with dimensions (W, L) is formed between N -period-long Bragg reflectors with a pitch Λ . More specifically, each period of the reflector consists of two segments ($\Lambda = L_1 + L_2$) with widths $W_1 \equiv W$ and W_2 , respectively. Clearly, for a recess grating like the one in Fig. 2 it holds $W_2 < W_1$, while for a protruding grating it would be $W_2 > W_1$. The cavity is side-coupled to a standard CGS waveguide ($w = 200$ nm) through a coupling gap g . The waveguide interacts with the resonator for a length equal to the extent of the cavity (L), after which the waveguide is curved away from the resonator in order to avoid coupling along the grating regions. An R value of $2 \mu\text{m}$ is adopted, for which radiation losses are negligible (Ketzaki et al 2013). The cavity (W, L) and grating $(W_1 \equiv W, W_2, \Lambda)$ geometrical parameters, as well as the coupling gap g , will be determined in Section 5 after identifying the design specifications in Section 4. For the number of grating periods, we fix N at 16, having verified it constitutes a favorable compromise between high reflectivity and compactness.

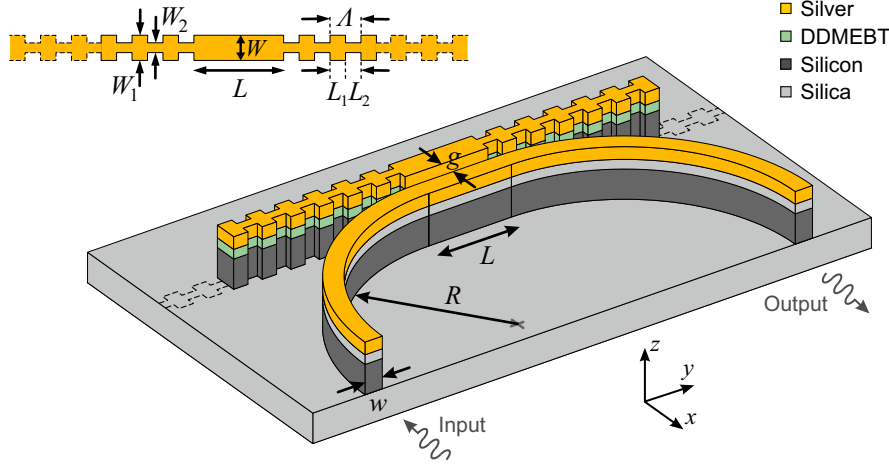


Fig. 2 NLCGS-based Bragg-grating resonator coupled to a CGS bus waveguide through coupling gap g . A cavity with dimensions (W, L) is formed between N -period-long Bragg reflectors with a pitch Λ . The waveguide is curved ($R = 2 \mu\text{m}$) to avoid coupling along the grating region.

3 Modeling framework

First, we briefly discuss the modeling framework employed. The nonlinear response of the resonator-waveguide system is studied with a theoretical framework combining perturbation theory and temporal coupled-mode theory (Soljačić et al 2002; Bravo-Abad et al 2007). This approach is much simpler compared to rigorously simulating the three-dimensional *nonlinear* system and still produces very accurate results, as has been demonstrated with photonic crystal cavities (Soljačić et al 2002; Yanik et al 2003; Bravo-Abad et al 2007). Rigorous full-wave simulations of the 3D system still need to be performed in order to feed the theoretical model, albeit they are conducted in the *linear* regime. In this work, these simulations are carried out with the 3D-VFEM (Tsilipakos et al 2011).

This framework has already been developed and successfully applied to side-coupled standing-wave cavities in the context of photonic crystal structures (Yanik et al 2003). However, the derived closed-form expression describing the CW nonlinear response assumes an infinite intrinsic quality factor for the resonator, as is typically the case with photonic crystal cavities. Here, we outline the formulation for the purpose of arriving at a general closed-form expression, valid for finite intrinsic quality factors and arbitrary coupling conditions. This generalization is necessary for studying plasmonic resonators which are inherently lossy.

Applying perturbation theory, the resonance shift due to Kerr nonlinearity can be cast in the form (Bravo-Abad et al 2007)

$$\frac{\Delta\omega}{\omega_0} = -\frac{1}{4}c_0 \left(\frac{\omega_0}{c_0}\right)^3 \kappa n_2^{\max} W_{\text{res}}, \quad (1)$$

where $W_{\text{res}} = (\epsilon_0/2) \iiint_V n^2(\mathbf{r}) |\mathbf{E}_0|^2 dV$ is the total energy stored in the cavity (on resonance stored electric and magnetic energies are equal), with $\mathbf{E}_0(\mathbf{r})$ denoting the unperturbed electric field in the structure. In Eq. (1) we have introduced the nonlinear feedback parameter κ ; a parameter measuring the overlap between nonlinear material and field distribution. It is

defined through (Bravo-Abad et al 2007; Soljačić et al 2002)

$$\kappa \triangleq \left(\frac{c_0}{\omega_0}\right)^3 \frac{\frac{1}{3} \iiint_V n_2(\mathbf{r}) n^2(\mathbf{r}) \left[|\mathbf{E}_0 \cdot \mathbf{E}_0|^2 + 2 |\mathbf{E}_0|^4 \right] dV}{\left[\frac{1}{2} \iiint_V n^2(\mathbf{r}) |\mathbf{E}_0|^2 dV \right]^2 n_2^{\max}}, \quad (2)$$

with n_2^{\max} being the maximum value of $n_2(\mathbf{r})$. κ is a dimensionless parameter inversely proportional to the effective mode volume. Moreover, it is independent of the nonlinear material (due to the normalization with n_2^{\max}), the peak power and the external quality factor as long as they do not dramatically affect the mode profile.

The Kerr-induced frequency shift $\Delta\omega$ of Eq. (1) can be readily introduced in a temporal CMT framework (Haus 1984; Fan et al 2003). Then, the equations describing a side-coupled standing-wave resonator are given by

$$\frac{da}{dt} = j(\omega_0 + \Delta\omega)a - \frac{1}{\tau_i}a - \frac{1}{\tau_e}a + j\sqrt{\frac{1}{\tau_e}}s_{\text{in}}, \quad (3a)$$

$$s_{\text{out}} = s_{\text{in}} + j\sqrt{\frac{1}{\tau_e}}a, \quad (3b)$$

$$s_{\text{ref}} = j\sqrt{\frac{1}{\tau_e}}a, \quad (3c)$$

where $a = a(t)$ is the mode amplitude, normalized so that $|a|^2 = W_{\text{res}}$. In the same way, input (s_{in}), output (s_{out}) and reflected (s_{ref}) wave amplitudes are normalized so that $|s|^2$ expresses guided power. Finally, $\tau_{i,e}$ denote intrinsic and external (coupling) photon lifetimes, respectively, associated with the respective quality factors through $Q = \omega_0 \tau / 2$.

Assuming a harmonic time dependence ($\exp\{j\omega t\}$), we can calculate the steady state ($d/dt = 0$) transmitted and reflected power by substituting Eq. (3a) in (3b) and (3c), respectively, as

$$T \equiv \frac{P_{\text{out}}}{P_{\text{in}}} = \frac{r_Q^2 + (\delta - \tau_e \Delta\omega)^2}{(1 + r_Q)^2 + (\delta - \tau_e \Delta\omega)^2}, \quad (4a)$$

$$R \equiv \frac{P_{\text{ref}}}{P_{\text{in}}} = \frac{1}{(1 + r_Q)^2 + (\delta - \tau_e \Delta\omega)^2}. \quad (4b)$$

In Eqs. 4, $\delta = \tau_e(\omega - \omega_0)$ is the normalized detuning and $r_Q = \tau_e/\tau_i = Q_e/Q_i$ the *intrinsic loss factor*. The latter is the parameter that generalizes the analysis, encompassing the possibility of finite intrinsic quality factors. Clearly, in lossless cases $Q_i \rightarrow \infty$ and $r_Q = 0$.

In order to construct the hysteresis loop using Eqs. (4), we first need to express the stored energy (contained in $\Delta\omega$) in terms of input, output and/or reflected power. More specifically, by recalling the definition of the quality factor as the fraction between stored energy over dissipated power per optical cycle we can write $Q_e = \omega_0 W_{\text{res}}/P_e$, where P_e is the power decaying to the neighboring waveguide. Considering that a standing-wave resonator radiates equally in both directions of the bus waveguide, P_e can be expressed in terms of reflected power as $P_e = 2P_{\text{ref}}$. Note that expressing P_e in terms of P_{out} instead of P_{ref} , as exercised in directly-coupled cavities (Soljačić et al 2002), would be desirable but is not possible. In side-coupled cavities P_{out} is not determined solely by the stored energy decaying to the

waveguide but by the power carried in the bus waveguide as well [Eq. (3b)]. Combining $Q_e = \omega_0 W_{\text{res}}/(2P_{\text{ref}})$ with Eq. (1), we get

$$\tau_e \Delta \omega = -\frac{P_{\text{ref}}}{P_0}, \quad (5)$$

where

$$P_0 = \frac{1}{\left(\frac{\omega_0}{c_0}\right)^2 \kappa Q_e^2 n_2^{\text{max}}} \quad (6)$$

is the characteristic power of the system. This parameter is of utmost importance, since it is associated with the threshold for bistability. Notice that P_0 is inversely proportional to the κQ_e^2 product. Obviously, in practical applications our goal is to minimize P_0 or, equivalently, maximize κQ_e^2 , in order to achieve low-power bistable action.

Using Eq. (5) in Eqs. (4) and introducing normalized guided powers $p = P/P_0$ we arrive at

$$\frac{p_{\text{out}}}{p_{\text{in}}} = \frac{r_Q^2 + (\delta + p_{\text{ref}})^2}{(1 + r_Q)^2 + (\delta + p_{\text{ref}})^2}, \quad (7a)$$

$$\frac{p_{\text{ref}}}{p_{\text{in}}} = \frac{1}{(1 + r_Q)^2 + (\delta + p_{\text{ref}})^2}. \quad (7b)$$

Eqs. (7) constitute a closed-form, 2×2 system of polynomial equations describing the CW nonlinear response and allowing for constructing the hysteresis loop. The system can only be decoupled in the case of infinite intrinsic quality factor, where intrinsic losses are zero and p_{ref} can be expressed in terms of input and output powers as $p_{\text{ref}} = p_{\text{in}} - p_{\text{out}}$. Then, Eq. (7a) can be used for describing the optical response, as in (Yanik et al 2003).

Eq. (7b) predicts bistable behavior for the reflected power when it admits three real, positive solutions. These solutions are inherited in Eq. (7a), giving the same bistable behavior in the output. From a mathematical perspective, bistability occurs when the slope of the $p_{\text{ref}} - p_{\text{in}}$ curve is infinite, indicating that more than one solution for the same abscissa is possible. This is expressed as $\partial p_{\text{ref}}/\partial p_{\text{in}} \rightarrow \infty$, or equivalently $\partial p_{\text{in}}/\partial p_{\text{ref}} = 0$. Applying the latter in Eq. (7b) we reach

$$3p_{\text{ref}}^2 + 4\delta p_{\text{ref}} + [\delta^2 + (1 + r_Q)^2] = 0. \quad (8)$$

Bistability occurs when the discriminant of Eq. (8) is positive (guided power must be a real number) and moreover $\delta < 0$ (ensures that the roots are positive numbers), leading to the condition

$$\delta < -(1 + r_Q)\sqrt{3} \equiv -\delta_{\text{th}}. \quad (9)$$

Equation (9) states that bistability manifests (for appropriate input power levels) when the normalized detuning is negative and exceeds the threshold value of $(1 + r_Q)\sqrt{3}$. Note that δ_{th} depends on r_Q ; it reduces to the constant value of $\sqrt{3}$ only in the lossless case.

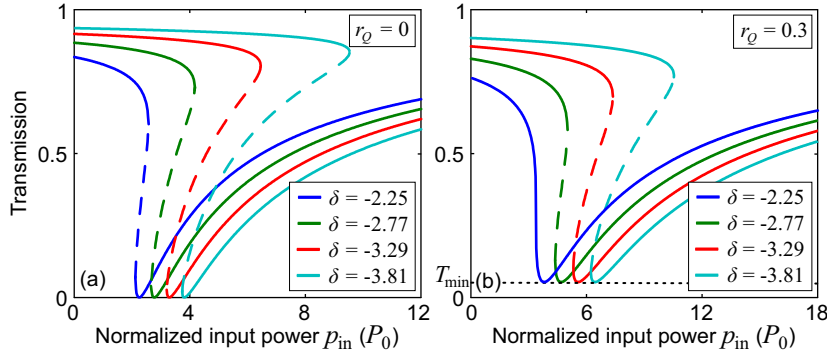


Fig. 3 Effect of detuning on optical response. (a) $r_Q = 0$ with the respective threshold being $\delta_{th} = \sqrt{3} \approx 1.73$, (b) $r_Q = 0.3$ with the respective threshold being $\delta_{th} = 1.3\sqrt{3} \approx 2.25$. Solid lines represent stable states, whereas dashed lines represent unstable states (although predicted by Eqs. (7) they cannot be practically observed). As $|\delta|$ increases, bistability manifests for higher input powers.

4 Effect of model parameters on bistability curve

Let us now investigate the effect of parameters δ and r_Q on the optical response for the purpose of identifying the values that lead to optimum performance. We are interested in low input power thresholds and high extinction ratios between bistable states.

We first examine the effect of normalized detuning δ . For this purpose, we fix r_Q at two distinct values, namely, $r_Q = 0$ and $r_Q = 0.3$, representing the absence and presence of intrinsic losses, respectively. In physical system terms, a photonic crystal cavity stands for the lossless case and a plasmonic cavity for the lossy. The results are depicted in Fig. 3 for four different detuning values: $\delta = \{-2.25, -2.77, -3.29, -3.81\}$. Note that these detunings correspond to different values in δ_{th} units for the two cases, since δ_{th} depends on r_Q [Eq. (9)]. For example, $\delta = -2.25$ corresponds to $-1.3\delta_{th}$ for $r_Q = 0$ and $-\delta_{th}$ for $r_Q = 0.3$. Obviously, for the latter case bistability cannot manifest as is evident from Fig. 3(b).

In both cases, the basic trends are the same. When detuning increases (in absolute value), the input power threshold increases as well. In the lossless case for example [Fig. 3(a)], for the lowest detuning considered bistability manifests at $2.3P_0$, while for the highest at $4P_0$. Moreover, note that with increasing detuning the hysteresis loop becomes wider and the maximum transmission level increases leading to lower insertion losses ($IL = 10 \log T_{max}$). The latter can be explained by the fact that for higher detuning values the operating wavelength falls farther away from the unperturbed resonant frequency, meaning higher transmission in the linear regime. Obviously, retaining the input power threshold at low values is essential. A good compromise between low power threshold, satisfactory loop span, and low insertion losses is attained for detunings in the range $\{-1.3\delta_{th}, -1.9\delta_{th}\}$, corresponding to $\{-2.25, -3.29\}$ for $r_Q = 0$.

Importantly, in the case of lossless structures ($r_Q = 0$) there is always a point in the low-transmission branch where the transmission is zero, leading to theoretically infinite ER between bistable states. On the other hand, for $r_Q = 0.3$ the minimum-transmission level elevates ($T_{min} \approx 0.05$), limiting the ER to finite values. This elevation is a result of the finite Q_i value; note that it depends solely on r_Q and not on δ , as the horizontal dotted line in Fig. 3(b) indicates.

In order to further understand this behavior, we examine the effect of r_Q on the bistability curve by fixing the detuning to a constant value. Three distinct values of r_Q are considered

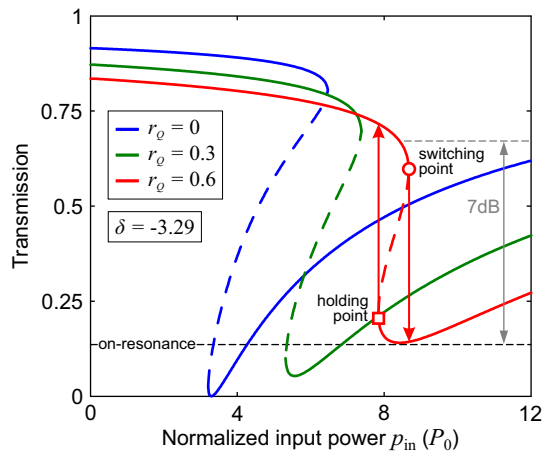


Fig. 4 Effect of intrinsic loss factor r_Q on optical response. The detuning parameter is kept constant at $\delta = -3.29$. As r_Q increases, the ER between bistable states deteriorates and bistability manifests for higher input powers. For the $r_Q = 0.6$ curve, characteristic points and states are clearly marked to support the relevant discussion in the text.

($r_Q = \{0, 0.3, 0.6\}$) with the results depicted in Fig. 4. The detuning is set to -3.29 to ensure that it exceeds δ_{th} for all cases of r_Q considered. One can readily observe that as r_Q increases, corresponding to lower Q_i values (Q_e is considered constant to enable normalizing with a common characteristic power P_0), the level of minimum transmission increases limiting the available ER between bistable states. This behavior is inherited from the linear regime: in the presence of intrinsic losses the transmission of a side-coupled standing-wave resonator does not vanish on resonance as is the case with lossless systems. This is a distinct trait of standing-wave resonators; in traveling-wave resonators irrespective of the level of intrinsic losses one can always get vanishing transmission on resonance by satisfying the critical coupling condition. Note also that the level of maximum transmission decreases (due to the decrease of δ in δ_{th} units), further contributing to ER degradation. The maximum achievable ER drops below the 10 dB limit for $r_Q > 0.4$. For $r_Q = 0.6$ it is only 7 dB, Fig. 4(b).

Another effect of the r_Q increase on the bistability loop is the increase in input power threshold: for $r_Q = 0$ bistability manifests for $P_{in} = 3.6P_0$ whereas when $r_Q = 0.6$ for $P_{in} = 8P_0$. This can be explained as follows: as intrinsic losses increase, a greater portion of the energy coupled to the cavity is dissipated, meaning that less energy is available for inducing the nonlinear shift. As a result, higher input powers are needed to reach the “switching point” (marked in Fig. 4 with a circle) where the cavity becomes resonant with the operating wavelength and a drop to the low-transmission branch occurs. Furthermore, as r_Q increases the detuning decreases in δ_{th} units. This means that the span of the hysteresis loop must decrease, as demonstrated in Fig. 3. Therefore, the “holding point” (marked in Fig. 4 with a square), corresponding to the minimum power required to remain on-resonance and thus on the low-transmission branch, experiences an even more pronounced shift towards higher input powers than the switching point. It is this shift of the holding point that is responsible for the increase in bistability threshold.

5 System design

In this section, we design the physical system based on the findings of Sections 3 and 4 using the 3D-VFEM. Specifically, we are interested in a system featuring minimum characteristic power P_0 , high ER between bistable states and low input power threshold for bistability.

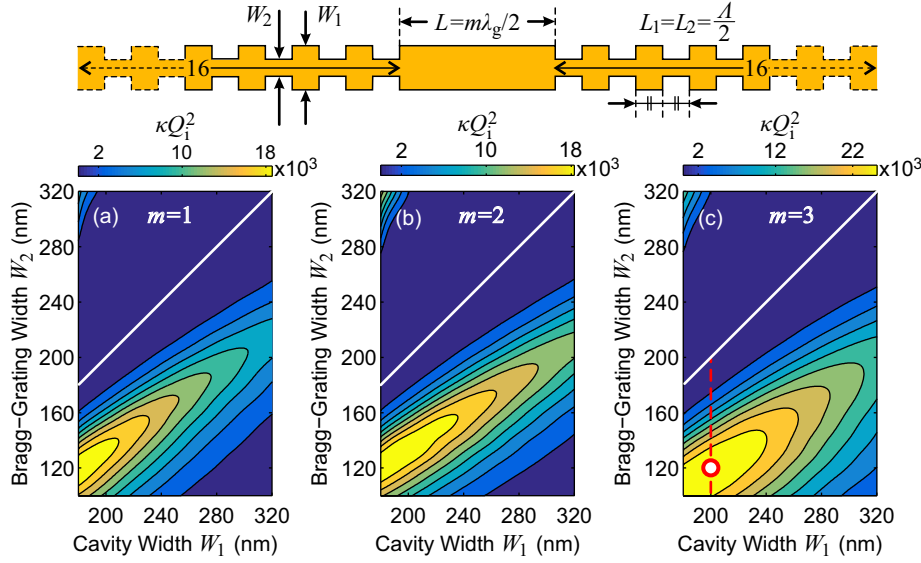


Fig. 5 Parametric analysis with respect to (W_1, W_2) : the κQ_i^2 product is evaluated for the three lowest-order modes ($m = 1, 2, 3$). For each width combination, lengths L and $L_1 = L_2$ are properly tuned for resonance at $\lambda_0 = 1.55 \mu\text{m}$. The optimum point is marked with a circle and corresponds to $(W_1, W_2) = (200, 120)$ nm and $m = 3$. Diagonal solid lines indicate the boundary between recess grating ($W_2 < W_1$) and protruding grating regions ($W_2 > W_1$). Inset: Top view of the Bragg-grating resonator with relevant geometric parameters.

The demand for minimum P_0 translates to maximum κQ_e^2 product [Eq. (6)], meaning that high values of Q_e are required. On the other hand, for a fixed (finite) intrinsic quality factor, high Q_e values lead to high r_Q values with a detrimental effect on ER and input power threshold (Fig. 4). We are thus seeking the highest r_Q value for which the ER between bistable states remains higher than 10 dB, since this is essential for practical applications. Considering that $r_Q < 0.4$ for ER > 10 dB (Section 4), we chose $r_Q = 0.3$ which in conjunction with $\delta = -3.29 = -1.46\delta_{\text{th}}$ leads to an ER of 11.7 dB and a bistability power threshold of $5.5P_0$.

Having set r_Q equal to a constant value, we can minimize the characteristic power P_0 by maximizing κQ_i^2 , instead of κQ_e^2 . To this end, we study the uncoupled resonator as an eigenvalue problem (in the linear regime). We conduct a parametric analysis with respect to W_1 and W_2 , in order to identify the optimum width combination. More specifically, we vary W_1 in the range 180 – 320 nm and W_2 in the range 100 – 320 nm and evaluate the corresponding κQ_i^2 product, Fig. 5. W_1 values beyond 320 nm are not considered in order to ensure single-mode operation of the underlying waveguide and avoid beating effects in the grating. For each (W_1, W_2) combination, we solve for the three lowest-order cavity modes by tuning the cavity length to an integer multiple of $\lambda_g/2$:

$$L = m \frac{\lambda_g}{2} = m \frac{\lambda_0}{2 \text{Re}\{n_{\text{eff},1}\}}, \quad (10)$$

where m denotes the order of the resonant mode.

Note that special care is exercised to ensure that each (W_1, W_2) combination results in a Bragg resonator that meets the necessary conditions for resonance at the desired frequency (λ_0 is set to $1.55 \mu\text{m}$). Besides properly adjusting the cavity length, this means specifying

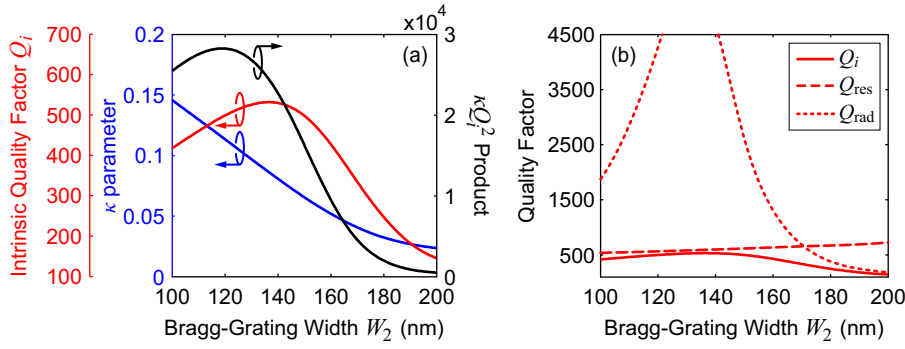


Fig. 6 (a) Quantities Q_i , κ , and κQ_i^2 along the dashed line in Fig. 5(c). The maximum κQ_i^2 product is attained for $W_2 = 120$ nm ($W_1 = 200$ nm). (b) Decomposition of Q_i into Q_{res} and Q_{rad} . Q_i is bound by resistive (radiation) losses at lower (higher) W_2 values.

lengths (L_1, L_2) to meet the Bragg condition, which, for first-order gratings, is written as

$$\text{Re}\{n_{\text{eff},1}\}L_1 + \text{Re}\{n_{\text{eff},2}\}L_2 = \frac{\lambda_0}{2}. \quad (11)$$

This is necessary since each (W_1, W_2) pair corresponds to different $(n_{\text{eff},1}, n_{\text{eff},2})$ values. Note that in all cases we opt for $L_1 = L_2 = \Lambda/2$.

The results for the three lowest-order modes ($m = 1, 2, 3$) are depicted in Fig. 5(a)-(c). It is clear that the κQ_i^2 product attains high values for recess gratings ($W_2 < W_1$) rather than protruding ones ($W_2 > W_1$) (the boundary between the two regions is marked with a white line). The optimum combinations of (W_1, W_2) lie in the small width region (lower left corner), where the κ parameter is high due to the reduced effective mode volume ($\kappa \propto 1/V_{\text{eff}}$). In addition, one can readily verify that the third-order mode leads to higher values of κQ_i^2 compared to the other ones. This is due to reduced radiation losses (resistive losses are constant irrespective of the cavity length). Higher order modes have also been examined, failing, however, to achieve higher products and are, thus, not presented. Focusing on the third-order mode [Fig. 5(c)], we chose the combination (200, 120) nm, since it lies in the region of high κQ_i^2 values and, moreover, the width of 200 nm complies with the standard width values of standard CGS waveguides (Wu et al 2010).

In order to gain better insight into the effect of width W_2 on the κQ_i^2 product, we examine κQ_i^2 along the dashed line in Fig. 5(c), which corresponds to $W_1 = 200$ nm and $W_2 < W_1$. The product variation is depicted in Fig. 6(a), along with the respective behavior of each quantity. On one hand, κ monotonically decreases with W_2 due to the increase in mode volume: a less pronounced corrugation results in a lower reflection coefficient and, consequently, in stronger field penetration into the grating. On the other hand, Q_i exhibits a non-monotonic behavior, peaking for $W_2 \approx 140$ nm and decreasing for higher values. In total, the κQ_i^2 product, adopting the non-monotonic behavior of Q_i , peaks for a W_2 value of 120 nm.

Let us now examine the behavior of Q_i in detail. Obviously, in a lossy, open resonator like the one examined, intrinsic losses are composed of resistive and radiation losses. For the respective quality factors: $Q_i^{-1} = Q_{\text{res}}^{-1} + Q_{\text{rad}}^{-1}$. Q_{rad} can be calculated by momentarily neglecting resistive losses, i.e., setting $\text{Im}\{\epsilon_{\text{Ag}}\} = 0$, and then used to calculate Q_{res} . All three quality factors are depicted in Fig. 6(b). Notice that Q_i is bound by resistive (radiation) losses at lower (higher) W_2 values. More specifically, Q_{res} varies in the range 500 – 720.

The increase with W_2 can be explained by the fact that for the underlying NLCGS waveguide resistive losses decrease with width. For the limiting value $W_2 = W_1 = 200$ nm the corrugation vanishes and the Bragg-grating resonator reduces to a Fabry-Pèrot (FP) cavity with a total length of $16\Lambda + L + 16\Lambda$. In such cases, Q_{res} can be directly estimated from the field profile of the underlying waveguide, as demonstrated in Appendix A. Returning to Fig. 6(b), Q_{rad} exhibits a much more pronounced variation compared to Q_{res} . It peaks at 130 nm, where both high grating reflectivity and reduced scattering at the cavity-grating interfaces are achieved. Lower W_2 values result in increased scattering at the cavity-grating interfaces, whereas higher W_2 values lead to reduced grating reflectivity, permitting a significant portion of power to be radiated at the grating ends. For $W_2 > 170$ nm, radiation losses are substantially increased and become the factor limiting Q_i , instead of resistive losses.

Having concluded the design of the uncoupled resonator, the complete set of geometrical parameters are $(W_1, W_2) = (200, 120)$ nm, $L = 1 \mu\text{m}$ ($3\lambda_g/2$), and $L_1 = L_2 = \Lambda/2 = 175$ nm. The resonator is characterized by $\kappa = 0.11$ and $Q_i = 500$, with $Q_{\text{res}} = 560$ and $Q_{\text{rad}} = 4300$ (Fig. 6). By employing the definition in (Tsilipakos and Kriezis 2014) we can obtain the effective mode volume: $V_{\text{eff}} = 0.1 \mu\text{m}^3$. Note that this value is 5 times smaller than that of the disk resonator in (Tsilipakos and Kriezis 2014). As anticipated, the Bragg resonator is able to confine the optical mode in small volumes, due to its standing-wave nature. This results in high values of κ , promising to reduce the power threshold. However, the intrinsic quality factor, which appears squared in Eq. (6), is limited to 500, whereas the NLCGS-based disk resonator in (Tsilipakos and Kriezis 2014) features a quality factor of 1750. This has a detrimental effect on power threshold, which becomes even more pronounced by the fact that for standing-wave resonators it is $Q_e < Q_i$ that appears in the power threshold expression, in contrast with the traveling-wave case. The characteristic power for the Bragg resonator is $P_0 = 1.34$ W, approximately 6 times higher compared to the disk.

The inability of the proposed structure to achieve higher quality factors can be attributed to the lack of a beneficial compromise between radiation and resistive losses. In contrast to radiation losses, which can be reduced by proper design [Fig. 6 (b)], the resistive ones consist an inevitable bottleneck toward the realization of high quality factors. A closed-form relation calculating Q_{res} for a lossy Fabry-Pèrot resonator, i.e., a standing-wave resonator comprised of a uniform nanophotonic waveguide segment between (partially) reflecting mirrors, is derived in Appendix A. Using this relation to obtain an estimate of the quality factor anticipated in our Bragg resonator implementation we find a value of 720, consistent with the value for $W_2 \rightarrow 200$ nm in Fig. 6 (b). Note, finally, that the high value of Q_{rad} obtained verifies that the number of periods selected ($N = 16$) is a sound choice. There is no need to employ more periods, since it is resistive losses that limit the Q_i value.

The last step in the design process is specifying the coupling gap g between resonator and waveguide. As already mentioned, the value of g should satisfy $r_Q = 0.3$, in order to obtain an ER exceeding 10 dB. By solving the eigenvalue problem for the coupled resonator, the loaded quality factor Q_ℓ is calculated as a function of g in the range 0.1-0.5 μm [Fig. 7(a)]. Then, we can determine Q_e through $Q_\ell^{-1} = Q_i^{-1} + Q_e^{-1}$ and, subsequently, r_Q . The condition $r_Q = 0.3$ is satisfied for a coupling gap of 210 nm. In Fig. 7(b) the electric field distribution is plotted at the xy plane halfway inside the polymer layer. Notice the third-order mode supported by the cavity. The mode decays to the neighboring waveguide towards both directions. As a result, a standing-wave pattern is formed along the interaction region. In the arced waveguide segments no coupling with the resonator is possible and a traveling wave is observed.

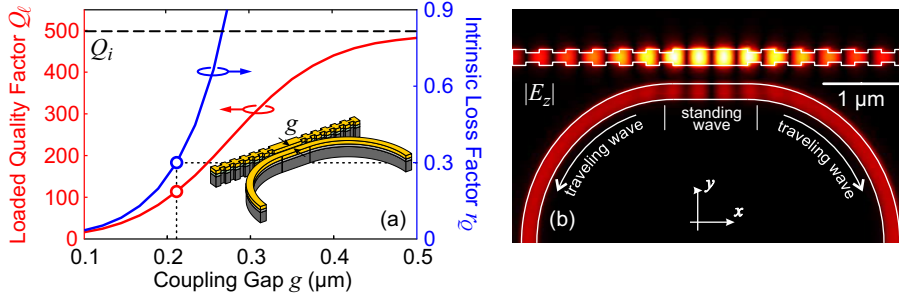


Fig. 7 (a) Loaded quality factor Q_L and intrinsic loss factor $r_Q = Q_L/Q_i$ as a function of the coupling gap g . As the coupling gap increases, Q_L approaches the unloaded (intrinsic) value marked with a dashed line. The condition $r_Q = 0.3$ is satisfied for a coupling gap of 210 nm. (b) Absolute value of dominant E -field component ($|E_z|$) at the xy plane halfway inside the polymer layer.

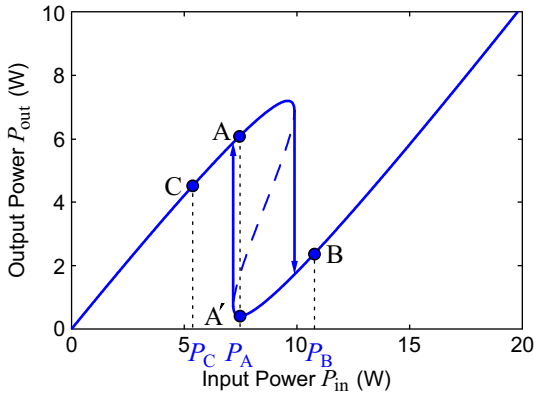


Fig. 8 Bistability curve for the proposed Bragg-grating cavity. The operating wavelength is 1567 nm. For $P_{\text{in}} = P_A = 7.5$ W the system exhibits states A and A' with an ER of 11.7 dB. Points B and C are used in Fig. 9 for toggling between them.

6 Performance Assessment

Having designed the Bragg-grating resonator, we can assess its performance. In Fig. 8 we plot the bistability curve for the optimum configuration: $r_Q = 0.3$ and $\delta = -3.29$ corresponding to an operating wavelength of 1567 nm. This time we plot the output power against P_{in} , instead of the transmission. Both axes are denormalized with $P_0 = 1.34$ W, specified in Section 5. Bistable states (A and A') with an ER of 11.7 dB appear at an input power of $P_A = 7.5$ W. Switching between them can be accomplished through points B and C which lie beyond and below the bistability regime, respectively. This is shown in Fig. 9, where basic memory operation is demonstrated with set and reset pulses. More specifically, second-order super-gaussian pulses with a FWHM of 1.2 ps are utilized to toggle the system state. The first pulse toggles the system to the low-output state (A') by following the route ABA' on the bistability curve. The application of a second pulse (which is actually a dip in input power) returns the system to the high output state (A) through point C. Importantly, in both transitions the cavity responds in approximately 2 ps, rendering the proposed structure suitable for ultrafast memory/switching applications.

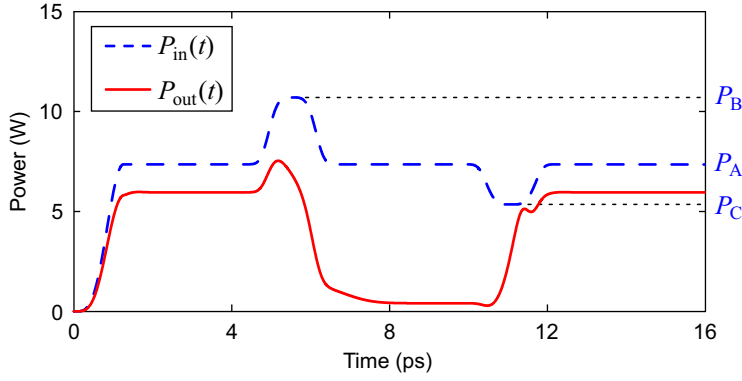


Fig. 9 Temporal response of the proposed Bragg resonator. The first pulse toggles the system to the low output state following the route ABA' on the bistability curve. The second pulse returns the system to the high-output state through the $A'CA$ route. In both cases, the response time is approximately 2 ps. Points A, A' , B and C are clearly marked in Fig. 8.

In Fig. 9 the dynamic response has been obtained by using Eqs. (3a) and (3b). More specifically, using Eqs. (1) and (5), Eq. (3a) transforms into

$$\frac{d\tilde{a}}{dt} = -j \left(\omega - \omega_0 + \frac{1}{\tau_e^2 P_0} |\tilde{a}|^2 \right) \tilde{a} - \left(\frac{1}{\tau_i} + \frac{1}{\tau_e} \right) \tilde{a} + j \sqrt{\frac{1}{\tau_e}} \tilde{s}_{in}, \quad (12)$$

where \tilde{a} and \tilde{s} denote slowly varying envelope functions. After calculating \tilde{a} through Eq. (12), $\tilde{s}_{out} = \tilde{s}_{in} + j\sqrt{1/\tau_e} \tilde{a}$, i.e., Eq. (3b), is used to obtain the output power.

7 Conclusion

To summarize, we have proposed a hybrid plasmonic Bragg-grating resonator for optical bistability. The structure is compact and can be readily interfaced with standard silicon-photonics waveguides. It offers tight mode confinement with the effective mode volume of the supported mode being only $0.1 \mu\text{m}^3 \approx 0.15(\lambda/n_D)^3$. Although mode volume is significantly reduced compared to traveling-wave implementations (Tsilipakos and Kriezis 2014), the power threshold could not be improved due to resistive losses limiting the quality factor to low values. More specifically, bistable operation with an ER of 11.7 dB requires an input power of 7.5 W.

It is thus expedient to examine alternative standing-wave resonator implementations for reducing the power threshold and matching, or even exceeding, the performance of traveling-wave resonators. To this end, photonic crystal implementations with 2D periodicity can be a favorable approach. More specifically, point-defect cavities with minimal penetration of the field components in the surrounding crystal structure could provide significantly reduced effective mode volumes and, thus, power thresholds.

In addition, since resistive loss constitutes the ultimate limiting factor for achieving low input power thresholds, it is worth examining alternative waveguiding configurations for the implementation of bistable components, based on both traveling- and standing-wave resonators. A promising candidate is long-range hybrid plasmonic waveguides (Bian and Gong 2014; Ma and Helmy 2014), which based on the principle of a symmetric waveguiding environment can exhibit very high propagation lengths.

Acknowledgements This work has been co-financed by the European Union (European Social Fund) and Greek national funds through the Operational Program “Education and Lifelong Learning” of the National Strategic Reference Framework: Research Funding Program THALES “Reinforcement of the interdisciplinary and/or inter-institutional research and innovation” (Project ANEMOS).

A Appendix

Suppose we have a standing-wave resonator formed by any lossy nanophotonic waveguide segment bound by (partially) reflective mirrors, i.e., a generalized Fabry-Pèrot (FP) resonator. An implementation based on the NLCGS waveguide is depicted in Fig. 10(a). Our goal is to derive an expression for calculating Q_{res} by relying solely on the mode profile of the underlying waveguide, i.e., the solution of a 2D eigenvalue problem instead of a 3D one. This is possible since the structure is uniform along the z -axis.

Based on the definition of the quality factor, Q_{res} can be expressed as the ratio of the energy stored in the resonator to the energy dissipated per optical cycle due to ohmic (resistive) losses in the metal. Hence,

$$Q_{\text{res}} = \omega \frac{W_{\text{stored}}}{P_{\text{ohmic}}} = \omega_0 \frac{\iiint_V \left[\frac{1}{4} \text{Re} \left\{ \frac{d(\omega \varepsilon)}{d\omega} \right\} |\mathbf{E}(x, y, z)|^2 + \frac{1}{4} \mu |\mathbf{H}(x, y, z)|^2 \right] dV}{\iiint_V \frac{1}{2} \text{Re} \{ \mathbf{E}(x, y, z) \mathbf{J}^*(x, y, z) \} dV}, \quad (13)$$

where \mathbf{J} is the electric current density and V denotes the volume of the resonator. Any lossy materials (including metals) can be modeled using a complex dielectric constant and, thus, the electric current density can be written as $\mathbf{J} = \sigma \mathbf{E}(x, y, z) = \omega_0 \text{Im} \{ \varepsilon \} \mathbf{E}(x, y, z)$. If we additionally assume that the materials can be treated as non-dispersive, which is justified by the absence of material resonances near the operation wavelength of $1.55 \mu\text{m}$, Eq. (13) takes the form

$$Q_{\text{res}} = \frac{1}{2} \frac{\iiint_V [\text{Re} \{ \varepsilon \} |\mathbf{E}(x, y, z)|^2 + \mu |\mathbf{H}(x, y, z)|^2] dV}{\iiint_V \text{Im} \{ \varepsilon \} |\mathbf{E}(x, y, z)|^2 dV}. \quad (14)$$

Now, due to structure uniformity along the z -axis, the standing waveform $[\mathbf{E}(x, y, z), \mathbf{H}(x, y, z)]$ possesses a cross-sectional field distribution identical to the mode profile $[\mathbf{e}(x, y), \mathbf{h}(x, y)]$ of the underlying waveguide. In other words, we can write $\mathbf{E}(x, y, z) = \mathbf{e}(x, y) f(z)$ and $\mathbf{H}(x, y, z) = \mathbf{h}(x, y) f(z)$, where $f(z)$ is a scalar function denoting the standing-wave pattern. Separating the z -dependence and simplifying we arrive at

$$Q_{\text{res}} = \frac{1}{2} \frac{\iint_{S_m} [\text{Re} \{ \varepsilon \} |\mathbf{e}(x, y)|^2 + \mu |\mathbf{h}(x, y)|^2] dS}{\iint_{S_m} \text{Im} \{ \varepsilon \} |\mathbf{e}(x, y)|^2 dS}, \quad (15)$$

where S_m denotes the cross-section of metal regions. Note that the nominator and denominator in Eq. (15) represent stored and dissipated energies *per unit length*.

We have, thus, derived a closed-form expression allowing for calculating the resistive quality factor of a general waveguide-segment standing-wave resonator based on the solution of the two-dimensional eigenvalue problem of the underlying waveguide. For the purpose of testing the accuracy of the derived expression through an example, we consider the NLCGS-based resonator in Fig. 10(a). The $Q_{\text{res}}^{2\text{D}}$ values calculated by Eq. (15) are compared with the quality factors extracted from the complex eigenfrequency of the three-dimensional eigenvalue problem ($Q_{\text{res}}^{3\text{D}}$, Fig. 10(b)). Note that for the 3D problem we have considered perfectly-reflecting (PEC) mirrors. In this case, the resonator does not suffer radiation losses and Q_{res} coincides with Q_r . Obviously, the agreement is very good. Note that the two approaches are compared for a wide range of widths (180 – 380 nm) and two distinct h_D values (30 and 50 nm) to illustrate the validity of the approach.

Although Eq. (15) holds for cross-sectionally uniform standing-wave resonators, it is valuable for estimating Q_{res} in resonators with distributed reflectors as well. Clearly, the estimate is more accurate in cases of shallow grating corrugation or weak field penetration in the distributed reflectors. More specifically, in cases of shallow gratings the entire resonator length (including gratings) can be perceived as the FP cavity, since field penetration in the gratings is bound to be strong. Due to the small corrugation, the structure is nearly uniform. On the other hand, in cases of weak penetration, although the corrugation may be large, the mode is located primarily in the central region, which is obviously uniform. Here it is only the central part of

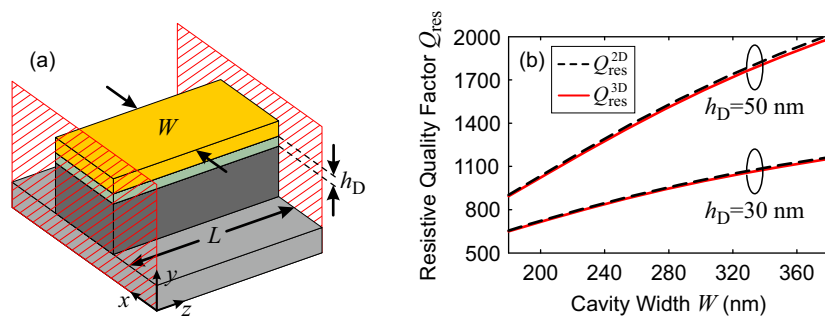


Fig. 10 (a) CGS-based standing-wave resonator consisting of a waveguide segment with dimensions W , L between (partially) reflective mirrors. (b) Resistive quality factor Q_{res} as a function of cavity width W for h_{D} values of 30 and 50 nm. The 2D approach of Eq. (15) is compared with the quality factor extracted from the complex eigenfrequency of a 3D eigenvalue problem. The close agreement between 2D and 3D calculations verifies the validity of Eq. (15).

the resonator that is perceived as the FP cavity. In both cases, the mode resides in a nearly-uniform region, meaning that an accurate estimate is anticipated.

As a final remark, the idea of a closed-form expression able to predict the Q factor of a standing-wave resonator by solving an eigenvalue problem of the underlying waveguide is actually familiar from transmission line theory (Pozar 2005). More specifically, the quality factor of a resonator formed by a closed- or open-circuited (TEM) transmission line segment, is approximated by $\beta/2\alpha$, where β (α) is the propagation (attenuation) constant of the underlying waveguide, calculated by solving the corresponding eigenvalue problem. Consequently, Eq. (15) can be thought of as a generalization of the $\beta/2\alpha$ relation. The former accounts for the complex nature of the hybrid nanophotonic modes, whereas the latter holds only for TEM or quasi-TEM waveguides (e.g., microstrips).

References

- Almeida VR, Lipson M (2004) Optical bistability on a silicon chip. *Opt Lett* 29(20):2387–2389
- Bian Y, Gong Q (2014) Long-range hybrid ridge and trench plasmonic waveguides. *Appl Phys Lett* 104(25):251,115
- Bravo-Abad J, Fan S, Johnson S, Joannopoulos JD, Soljačić M (2007) Modeling nonlinear optical phenomena in nanophotonics. *J Lightw Technol* 25(9):2539–2546
- Esembeson B, Scimeca ML, Michinobu T, Diederich F, Biaggio I (2008) A high-optical quality supramolecular assembly for third-order integrated nonlinear optics. *Adv Mater* 20(23):4584–4587
- Fan S, Suh W, Joannopoulos JD (2003) Temporal coupled-mode theory for the Fano resonance in optical resonators. *J Opt Soc Am A* 20(3):569–572
- Haus HA (1984) *Waves and Fields in Optoelectronics*. Prentice-Hall, New Jersey
- Johnson PB, Christy RW (1972) Optical constants of the noble metals. *Phys Rev B* 6(12):4370–4379
- Kauranen M, Zayats AV (2012) Nonlinear plasmonics. *Nat Photon* 6(11):737–748
- Ketzaki DA, Tsilipakos O, Yioultis TV, Kriezis EE (2013) Electromagnetically induced transparency with hybrid silicon-plasmonic traveling-wave resonators. *J Appl Phys* 114:113,107
- Koos C, Vorreau P, Vallaitis T, Dumon P, Bogaerts W, Baets R, Esembeson B, Biaggio I, Michinobu T, Diederich F, Freude W, Leuthold J (2009) All-optical high-speed signal processing with silicon-organic hybrid slot waveguides. *Nat Photon* 3(4):216–219
- Kriesch A, Ploss D, Wen J, Banzer P, Peschel U (2012) Nonlinear effects in subwavelength plasmonic directional couplers. In: *CLEO 2012: Conference on Lasers and Electro-Optics*, paper 6327055
- Ma W, Helmy AS (2014) Asymmetric long-range hybrid-plasmonic modes in asymmetric nanometer-scale structures. *J Opt Soc Am B* 31(7):1723–1729
- Milián C, Skryabin DV (2011) Nonlinear switching in arrays of semiconductor on metal photonic wires. *Appl Phys Lett* 98(11):111,104
- Pannipitiya A, Rukhlenko ID, Premaratne M (2011) Analytical theory of optical bistability in plasmonic nanoresonators. *J Opt Soc Am B* 28(11):2820–2826

- Pitilakis A, Kriezis EE (2013) Highly nonlinear hybrid silicon-plasmonic waveguides: analysis and optimization. *J Opt Soc Am B* 30(7):1954–1965
- Pitilakis A, Tsilipakos O, Kriezis EE (2012) Nonlinear effects in hybrid plasmonic waveguides. In: *ICTON 2012: 14th International Conference on Transparent Optical Networks* (IEEE, 2012), paper 6254436.
- Pozar DM (2005) *Microwave Engineering*, 3rd edn. John Wiley & Sons
- Shiu RC, Lan YC, Guo GY (2014) Optical multiple bistability in metal-insulator-metal plasmonic waveguides side-coupled with twin racetrack resonators. *J Opt Soc Am B* 31(11):2581–2586
- Soljačić M, Ibanescu M, Johnson SG, Fink Y, Joannopoulos JD (2002) Optimal bistable switching in nonlinear photonic crystals. *Phys Rev E* 66(5, art. no. 055601):055,601
- Tanabe T, Notomi M, Mitsugi S, Shinya A, Kuramochi E (2005) Fast bistable all-optical switch and memory on a silicon photonic crystal on-chip. *Opt Lett* 30(19):2575–2577
- Tsilipakos O, Kriezis EE (2014) Optical bistability with hybrid silicon-plasmonic disk resonators. *J Opt Soc Am B* 31(7):1698–1705
- Tsilipakos O, Pitilakis A, Tasolamprou AC, Yioultis TV, Kriezis EE (2011) Computational techniques for the analysis and design of dielectric-loaded plasmonic circuitry. *Opt Quantum Electron* 42(8):541–555
- Wang G, Lu H, Liu X, Gong Y, Wang L (2011) Optical bistability in metal-insulator-metal plasmonic waveguide with nanodisk resonator containing Kerr nonlinear medium. *Appl Opt* 50(27):5287–5290
- Wu M, Han Z, Van V (2010) Conductor-gap-silicon plasmonic waveguides and passive components at sub-wavelength scale. *Opt Express* 18(11):11,728–11,736
- Xiang Y, Cai W, Wang L, Ying C, Zhang X, Xu J (2014) Design methodology for all-optical bistable switches based on a plasmonic resonator sandwiched between dielectric waveguides. *Journal of Optics* 16(2):025,003
- Xu P, Shi Y (2013) High Q/V hybrid plasmonic photonic crystal nanobeam cavity: Towards low threshold nanolasers application. *Opt Commun* 311:234–238
- Xu Q, Lipson M (2007) All-optical logic based on silicon micro-ring resonators. *Opt Express* 15(3):924–929
- Yanik MF, Fan S, Soljačić M (2003) High-contrast all-optical bistable switching in photonic crystal micro-cavities. *Appl Phys Lett* 83(14):2739–2741